

Charge-Programmable Photopolymers for 3D Electronics via Additive Manufacturing

Zhen Wang, Junbo Wang, Zhenpeng Xu, Ryan Hensleigh, Haotian Lu, Mack Sowers, Marcus A. Worsley, Yahya Rahmat-Samii, and Xiaoyu (Rayne) Zheng*

Charge-programmed 3D printing enables the fabrication of 3D electronics with lightweight and high precision via selective patterning of metals. This selective metal deposition is catalyzed by Pd nanoparticles that are specifically immobilized onto the charged surface and promises to fabricate a myriad of complex electronic devices with self-sensing, actuation, and structural elements assembled in a designed 3D layout. However, the achievable property space and the material-performance correlation of the charge-programmed printing remain unexplored. Herein, a series of photo-curable resins are designed for unveiling how the charge and crosslink densities synergistically impact the nanocatalyst-guided selective deposition in catalytic efficiency and properties of the 3D printed charge-programmed architectures, leading to high-quality 3D patterning of solid and liquid metals. The findings offer a wide tunability of the structural properties of the printed electronics, ranging from stiff to extreme flexibility. Capitalizing on these results, the printing and successful application of an ultralight-weight and deployable 3D multi-layer antenna system operating at an ultrahigh-frequency of 19 GHz are demonstrated.

1. Introduction

Electronics with defined 3D metal-dielectric patterns are the core of a broad range of applications, such as antennas,^[1] actuators,^[2] sensors,^[3] integrated circuits,^[4] metamaterials,^[5] energy storage devices^[6] and more. Traditional fabrications of 3D circuits must rely on lithography,^[7] etching,^[8] or deposition,^[9] and typically only modify the surfaces of 3D objects with 2D conductive patterning rather than truly and inherently constructing 3D complex conducting pathways.^[10] Therefore, the designs are limited to relatively simple layouts with excessive structural materials,

and hence redundant weight.^[11] While additive manufacturing can fabricate complex 3D structural layouts from single-material components with only the necessary amount of feedstock, methods to fabricate arbitrary multi-material metal-dielectric layouts typical of electronics, which could potentially enable printing 3D circuits, antennas, functional devices, and batteries, are still rare.^[12]

Integrating multiple 3D printing systems for metal and dielectric materials could potentially enable the fabrication of 3D electronic devices.^[13] However, 3D printing of materials from different categories generally involves incompatible mechanisms for materials build-up.^[14] For example, dielectric polymers are mostly built up by fused deposition modeling or photo polymerization^[15] while metals are generally fused by laser from powders.^[16] The incompatibility poses a big challenge for the

fabrication of all-in-one multi-functional electronics with one single step. The 3D patterning catalyst that can trigger a following selective metal deposition has become a widely adapted approach (Table S1, Supporting Information). Active catalysts can be blended into resins and 3D printed with noncatalytic resins to achieve 3D patterns^[17] or written on printed structure^[18] to guide the following in situ metal deposition. Embedded catalyst precursors can be selectively activated by laser to trigger metal deposition.^[19] Fused filament fabricated conductive parts can also be electroplated with metal^[20] or induce selective metal deposition by the nucleation effect of the fillers.^[21] These approaches

Z. Wang, Z. Xu, H. Lu, M. Sowers, X. (Rayne) Zheng
 Department of Material Science and Engineering
 University of California
 Berkeley, CA 94720, USA
 E-mail: rayne23@berkeley.edu

Z. Wang, Z. Xu, R. Hensleigh, H. Lu, X. (Rayne) Zheng
 Department of Civil and Environmental Engineering
 University of California
 Los Angeles, CA 90095, USA

J. Wang, Y. Rahmat-Samii
 Department of Electrical and Computer Engineering
 University of California
 Los Angeles, CA 90095, USA

M. A. Worsley
 Materials Science Division
 Lawrence Livermore National Laboratory
 Livermore, CA 94550, USA

X. (Rayne) Zheng
 Materials Engineering Division
 Lawrence Berkeley National Laboratory
 Berkeley, CA 94720, USA

 The ORCID identification number(s) for the author(s) of this article can be found under <https://doi.org/10.1002/adfm.202313839>

© 2024 The Authors. Advanced Functional Materials published by Wiley-VCH GmbH. This is an open access article under the terms of the Creative Commons Attribution-NonCommercial License, which permits use, distribution and reproduction in any medium, provided the original work is properly cited and is not used for commercial purposes.

DOI: [10.1002/adfm.202313839](https://doi.org/10.1002/adfm.202313839)

involve a toolpath (such as a nozzle or laser rastering) or a substrate on which features are written. Toolpath necessitates longer printing time. The reliance on a substrate/board to write features limits the complexity of 3D topology and precludes the possibility of light-weighting.

Charge-programmed 3D printing fulfills selective and volumetric deposition of multiple functional materials, including metals, within arbitrary 3D complex layouts with a reduction in printing time and minimal processing steps for metal/dielectric 3D architectures with high resolution.^[22] This process starts with patterning curable dielectric and charged monomers in the designated space of the 3D structures. The charged area of the structure is further functionalized with a broad range of materials beyond metals, such as metal oxides, magnetic materials, carbon nanotubes, and piezoelectric materials. This method achieves high-precision printing of conductive materials on true 3D micro-architectures with micro-scale resolutions and has demonstrated applications in robotic actuation, sensing, and ultrasonic devices.^[22] However, the most fundamental aspects underpinning the process and material property trade-off are largely unexplored. This is especially challenging as these 3D electronics applications require high resolution, high uniformity, and satisfactory conductivity of the metal phase, as well as its adaptability for a wide range of dielectric materials with tunable mechanical properties, including stiff to soft polymers, high-temperature capability, as well as ceramics and composites. Understanding such trade-offs is critical to realize future 3D electronic devices with satisfactory performance and could potentially lead to the development of a series of novel materials compatible with this technique (high conductivity metal, liquid metal, ceramic, stretchable polymer, high-temperature polymer, etc.) for multiple intriguing electronic applications.

The direct 3D printing of antenna systems for electromagnetic wave manipulations is particularly fascinating due to the as-of-yet unexplored promising and deliverable vast design space.^[23] As the essential components of all radiofrequency equipment, antennas act as the interface between electromagnetic waves propagating through space and electric current signals in the backend circuitry. Patterning the metal phase with the highest possible conductivity, precision, and complexity in 3D space is crucial to fulfilling the designated interactions with the electromagnetic waves with a minimal ohmic loss.

In this study, we design the charge programmable photopolymers with a wide range of crosslink density, charge density, and chain flexibility to study their effects on the performance of 3D printed antennas. On the basis of the fine-tuned structures of the charge photopolymers, we realize control over the selective immobilization, size distribution, and embedding depth of the catalytic nanoparticles which play a key role in guiding the selective metal deposition and achieving optimal conductivity. Additionally, our method is compatible with liquid metal that can be comfortably patterned and allow larger deformation within a complex flexible 3D layout. With the implemented 3D lattice designs,^[24] we demonstrate the potential application of the nano catalyst-guided selective metal deposition in a deployable antenna. A set of strategies allows us to achieve optimal 3D printing of ultralight antenna with 3D patterned metallic/dielectric micro-architectures with tunable mechanical properties (from stiff to deployable antenna), compared to current antenna devices. Our

findings provide routes to simultaneously achieve the desired flexibility while retaining high conductivity, ultralight weight, as well as optimal electromagnetic beam steerability, for 3D printable all-in-one antenna devices.

2. Experimental Section

2.1. Multi-Material Printing

2.1.1. Resin Formulations

Negative resins were composed of trimethylpropane triacrylate (TMPTA) and bis(2-(methacryloyloxy)ethyl)phosphate (PDD) at weight ratios of 95/5, 90/10, 80/20, 70/30, 60/40, and 50/50, respectively. In addition, each formula contained 2% phenylbis(2,4,6-trimethylbenzoyl)phosphine oxide (Irg819) as the photoinitiator and 0.05% Sudan I as the photo absorber. Both are in wt.% to the total mass of TMPTA and PDD. The neutral resin was composed of polyethylene glycol diacrylate (PEGDA) with 2 wt.% of Irg819 and 0.05 wt.% of Sudan I.

Flexible negative resins were composed of ethylene glycol phenyl ether acrylate (PA) and PDD at weight ratios of 95/5, 90/10, and 80/20, respectively. Each formula consisted of 2 wt.% Irg819 as the photoinitiator and 0.05 wt.% Sudan I as the photo absorber. The flexible neutral resin was PA with 2 wt.% of Irg819 and 0.05 wt.% of Sudan I (yellow) or FormLabs flexible 80A (black).

Negative polyimide resin was composed of 78 g poly(pyromellitic dianhydride-co-4,4'-oxydianiline), amic acid solution (PMDAODA PAA, 15–16 wt.% in N-methylpyrrolidone), 4.84 g 2-(dimethylamino)ethyl methacrylate (DMAEMA, 0.5 equiv. in respect to the COOH groups of the PAA), 4.17 g PDD, and 0.33 g Irg819. The neutral polyimide resin contained 78 g PMDAODA PAA solution, 4.84 g DMAEMA, and 0.33 g Irg819.^[25] After multi-material printing, the structure was carefully dried and imidized according to the protocol by Herzberger et al.^[25] and then selectively deposited with copper.

The negative ceramic resin was formulated with lead zirconate titanate (PZT), PEGDA, and PDD in a volume ratio of 30/60/10 with 2.5 wt.% Irg 819 with respect to the total mass of PEGDA and PDD. The neutral resin was composed of PZT and PEGDA in a volume ratio of 35/65 with 2.5 wt.% Irg 819 to PEGDA. The resins were prepared using a high-energy ball mill EMAX (Retsch) at 1000 rpm for 30 min. After printing, the structure was selectively deposited with copper and then sintered according to the protocol described by Lu et al.^[26]

2.1.2. Printing

A custom bottom-up multi-material projection micro-stereolithography (μ SL) system^[22,27] was used to fabricate the octets presented in this work. First, a computer-aided design model was sliced into two different groups of enclosed images such that each group represented one material. The sliced images were subsequently digitalized and sent to a light engine which projected light of 405 nm wavelength through a group of lenses onto the corresponding resins, solidifying the resin into

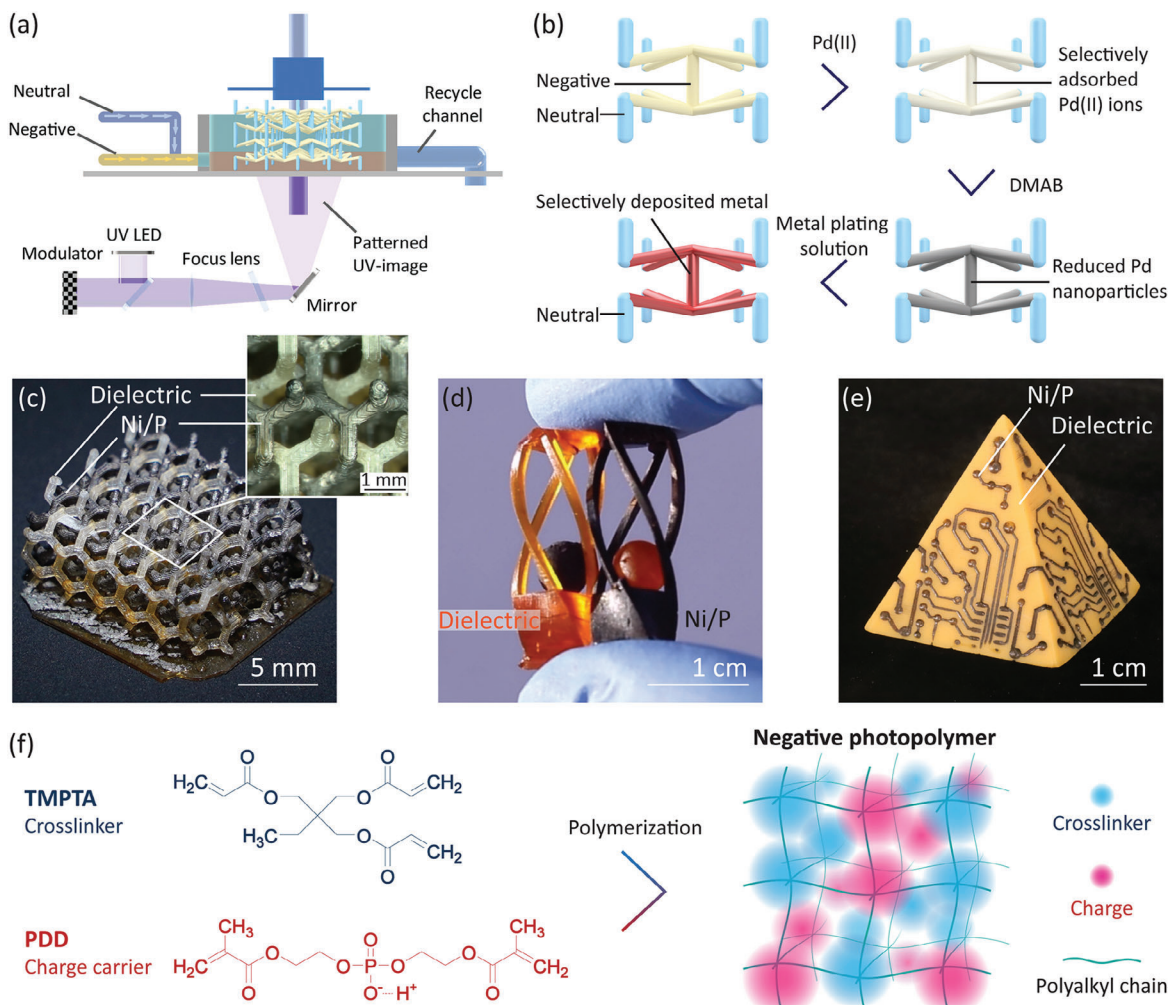


Figure 1. Charge programmed selective metal deposition. a,b) Schematic illustration of a) the 3D printing and b) the nano catalyst-guided selective Cu deposition process. c–e) Examples of selectively plated parts: c) a 3D interpenetrating lattice patterned with the selectively plated grey Ni/P alloy and the pale yellow dielectric, d) two sets of free-moving balls in cages with selectively plated Ni/P alloy, and e) a circuit on a 3D pyramid substrate.^[22] f) Composition and the figurative illustration of the structure of the negative photopolymer.

a solid layer bound to the building platform. The build platform elevates to replenish resin and repeat the cycle. A washing system was used when material changing was needed. While switching the resin, the printed parts were lifted vertically up from the resin in order to ensure the printing precision, and rinsed and blown dry. This process was repeated layer by layer, creating 3D structures with multiple resins.

The horn was 3D printed using the TMPTA/PDD 70/30 resin on a commercial printer (Anycubic Photon S), which had a lateral printing resolution of $\approx 50 \mu\text{m}$. The transmitarray was printed on the same printer (Anycubic Photon S).

2.2. Metal Plating

The selective plating procedure was adapted from the previous work with some optimizations to further improve the deposition quality. First, a negative resin and a neutral resin were 3D printed with a multi-material printing system. The printed parts

were soaked into Pd(II) solution (0.014 g Pd(II) salt dissolved in 10 g water) for 5 min to adsorb Pd(II) to the negative charge sites, followed by thorough rinsing with water and drying with compressed air. Then the parts were soaked in DMAB solution (0.006 g DMAB dissolved in 10 g water) for 5 min to reduce Pd(II) to Pd, followed by rinsing. Finally, the parts were submerged in Cu solution (1:1 mixture of Caswell electroless Cu A & B) for typically 1 h or otherwise specified reaction time to deposit Cu. For the Ni-P plated samples showcased in Figure 1, the final step was submerging the samples in Ni solution (1:3:16 mixture of Caswell electroless Ni A: B: water) for 1 h at 80 °C.

2.3. EGaIn Coating

EGaIn was stored in 0.1 M HCl solution before use. The acidic condition kept the liquid metal free of oxides. The parts selectively plated with Cu were dipped into the solution and the liquid metal wetted the surface of Cu immediately upon contact.

Then the excessive liquid metal was shaken off to get the neat EGaIn coatings.

2.4. Antenna Simulation and Measurement

In simulations, the dielectric material is modeled with a dielectric constant of 3.6 and a loss tangent of 0.02, which are estimated values for the resin used for printing. The transmitarray unit cell is designed in CST Studio. The antennas were measured in the spherical near-field antenna measurement range at the University of California, Los Angeles (UCLA).

3. Results and Discussion

3.1. Charge Programmed Feedstock for Selective Cu Deposition

The selective metal deposition on the additively manufactured structures relies on a charge-programmed multi-material stereolithography (SLA) technique,^[22] as schematically depicted in Figure 1a. The building substrate was alternately dipped into each resin with positive, negative, or neutral charge polarity so that the subdomain patterns with different polarities were solidified and bound to the previous layer. The process was repeated layer by layer, patterning multiple materials with different polarities into their designated coordination in 3D space (Figure 1b). The charges of the resins were inherited from the functional pendant groups of the photo monomers. Monomers with an amino pendant group carry a positive charge when binding a proton from water. Those with a carboxyl or phosphate group donate their proton and become negatively charged when soaked in water. Those without polar pendant groups stay neutral in the water. The charged surfaces spontaneously immobilize the oppositely charged catalyst species, driven by the thermodynamically favored entropy increase caused by the release of the small molecules of the counter ions. In this work, positively charged palladium ions, Pd(II), were absorbed by the negatively charged resins while the neutral resin composed of PEGDA had no interaction with Pd(II) (Figure 1b). The selectively immobilized Pd(II) were further reduced into Pd nano particles to catalyze the in situ deposition of a metal layer while the neutral resin remained uncoated (Figure S1, Supporting Information). We take advantage of projection SLA in high resolution (<50 μm) and large build areas (>100 cm² x-y footprint),^[28] rendering the printed objects high-resolution structures that can be deposited with conformal metals such as a Ni/P alloy as showcased in Figure 1c–e and Cu as the objective being studied in this work. The bonding between PEGDA and the negative resins is comparable with each of their single material counterparts. All gave strength in the mega pascal range as shown in Figure S2a,b (Supporting Information). When switching materials, rinsing the printed parts with ethanol induced a slight strength drop. This strength drop could be due to rinsing off some nonfully polymerized oligomers of the first printed material, causing induced micro pores that weaken the bonding strength (Figure S2c, Supporting Information). In comparison, wick dry is preferable in maintaining the strength of the interface where the residue oligomers of the first material may have the opportunity to mingle with the second material and

copolymerize to form a stronger interface (Figure S2d, Supporting Information).

As the substrate where the Cu deposition took place, the composition of the resin for negative photopolymer directly influences the performance of the plated Cu layer. To compose the negative resins, we selected two photo-monomers, TMPTA and PDD at different mass ratios from 90/10 to 50/50, Irg819 as the photo initiator, and Sudan I as the photo absorber. The photoinitiator released free radicals upon the 405 nm UV irradiation to start the photopolymerization. The photo absorber restricted the polymerizations within a certain range to avoid over-cure and ensured a high printing resolution. The two photo monomers had different functional groups and different numbers of carbon–carbon double bonds for polymerization which together tailored the polarity and crosslink density of the as-printed photopolymers. TMPTA has three carbon–carbon double bonds that can be polymerized, rendering a highly cross-linked rigid network. PDD was the charge carrier whose phosphate group disassociated in water and formed intimate ionic interaction with Pd(II). With two carbon–carbon double bonds, PDD provides a lower cross-link density than TMPTA. The figurative molecular structure of the negative resin composed of TMPTA and PDD is shown in Figure 1f. For the negative TMPTA/PDD resins, the increased TMPTA content leads to a more densely cross-linked negative photopolymer. As the PDD content increased, the amount of charge increased whilst the cross-link density decreased. The combination of the variations enabled a linearly increased water uptake as the PDD content increased, as shown in Figure S3 (Supporting Information). This indicates that a less cross-linked network with more charged phosphate groups allowed more water molecules permeating into the interior of the printed parts. Balancing the cross-link density and the charge density, we obtained materials with tunable catalyst efficiency, electrical conductivity, and mechanical properties.

3.2. Catalyst Immobilization

We first investigated the influence of crosslink degree and charge content of the negative photopolymers on the immobilization of nano Pd catalysts. This was the first and the most crucial step of the selective patterning process. The selective Cu deposition relied on the immobilization of the Pd(II) (positively charged) on the negative resin printed area. The cross-link density contributed mainly by TMPTA and partially by PDD determined the permeation of Pd(II) into the photopolymers and consequently, the embedding depth of Pd nanoparticles reduced in the following step. The charge density inherited from PDD determines the amount and size of the nanocatalyst that can be immobilized. After being reduced to metallic Pd nanoparticles with borane dimethylamine complex (DMAB), the surface of the negative photopolymer achieved catalytic activity and guided the electroless deposition of Cu to take place in the negative area.

By varying the ratio of TMPTA and PDD, the cross-link density of the negative photopolymers changed alongside the charge density, which synergistically affected the immobilization of the Pd catalyst. When the TMPTA/PDD ratio was higher than 95/5, no Pd could be localized on the surface of the negative photopolymers as shown in Figure 2a,b, and S4 (Supporting Information).

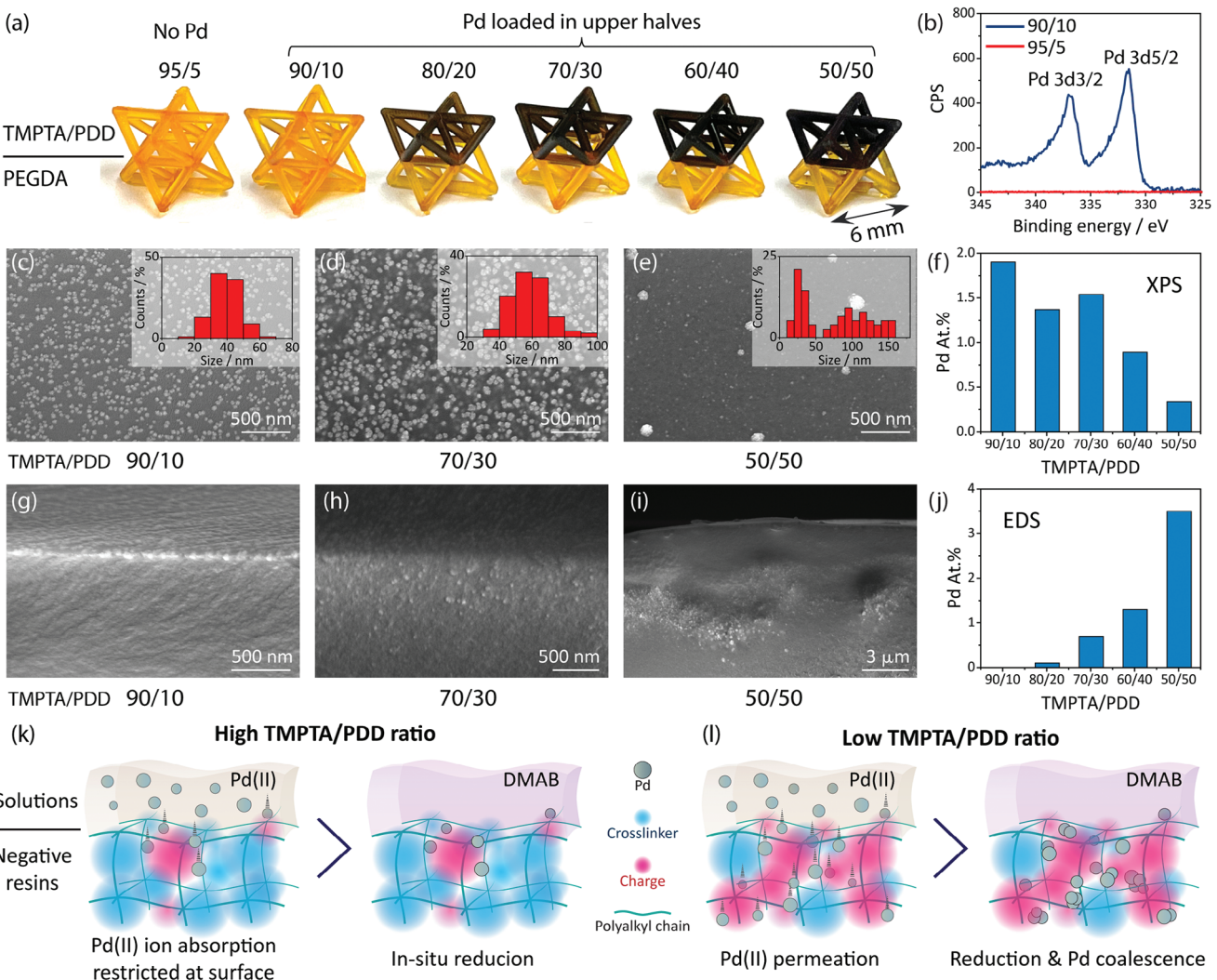


Figure 2. Pd catalyst immobilization. a) Photographs showing octets after the Pd immobilization treatment, of which the upper halves were printed using the negative resins and the bottom halves the neutral resin. A darker color indicates more and larger particles of Pd. b) High-resolution XPS spectra of element Pd that was immobilized on the negative photopolymers with different TMPTA/PDD compositions. c–e) Top-view SEM images of the Pd loaded surfaces of the TMPTA/PDD 90/10, 70/30, and 50/50 photopolymers, respectively (insets show the size distributions of the Pd particles). f) Atomic percentage of element Pd on the surfaces of the negative photopolymers determined by XPS. g–i) Cross-sectional SEM images of the fractured Pd loaded TMPTA/PDD 90/10, 70/30, and 50/50 photopolymers, respectively. j) Atomic percentage of element Pd on the surfaces of the negative photopolymers determined by EDS. k,l) Schematic illustrations showing the differences in catalyst absorption and reduction through the surfaces of photopolymers with k) high and l) low TMPTA/PDD ratios.

This is partially due to the inadequate surface charge density being unable to immobilize sufficient Pd(II). Additionally, the high cross-link density of the cured TMPTA/PDD 95/5 resin due to the high TMPTA content prevented Pd(II) from reaching the interior of the photopolymer. Therefore, Pd(II) could not be accumulated sufficiently to be reduced into nanoparticles to catalyze the Cu reduction. At a PDD content of 10%, the negative photopolymer could anchor Pd as detected by X-ray photoelectron spectroscopy (XPS, Figure 2b). The Pd nanoparticles had a fine and uniform particle size of 39 ± 9 nm (Figure 2c). Such a fine particle size cannot be visualized by eye/color change. Therefore, the Pd catalyst-loaded upper half of the 90/10 octet was able to retain the original color of the resin due to the existence of Sudan I (Figure 2a). With the PDD content increasing, the Pd nanoparticle size increased

up to 180 nm as shown in Figure 2c–e and Figure S4 (Supporting Information). The increase in particle size can also be easily distinguished by the darker color observed from the upper halves of octets with higher PDD contents (Figure 2a). The higher charge density of the negative photopolymers adsorbed a larger amount of Pd(II) which was reduced and aggregated non-uniformly into larger Pd nanoparticles. However, XPS, a surface-sensitive analysis technique,^[29] indicated that the atomic percentage of Pd unexpectedly decreased at a higher PDD content (Figure 2f; Table S2, Supporting Information). By observing the cross-sections, scanning electron microscopy (SEM) unveiled that the Pd nanoparticles were embedded deeper into the bulk of the negative photopolymer with a higher PDD content (Figure 2g–i), up to 4.5 μm deep in the TMPTA/PDD 50/50 photopolymer.

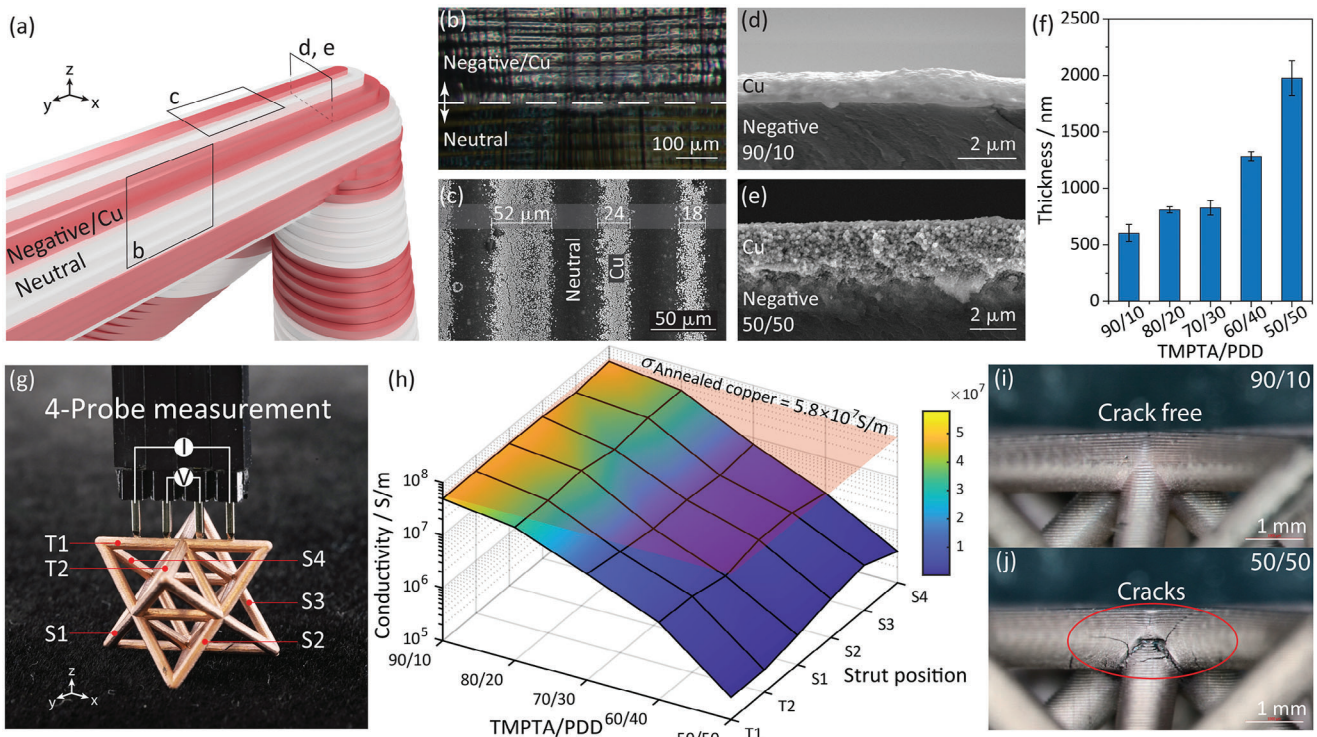


Figure 3. Cu deposition. a) Schematic of the joint of a lattice structure comprised of Cu-coated negative photopolymer and neutral photopolymer with the lettered boxes indicating the views of the following microscopic images. b) Microscopic image of the selectively plated Cu at the boundary of consecutively printed layers of the negative and neutral photopolymers. c) SEM image of the Cu deposited on a horizontally charge patterned surface showing the finest feature size achieved. d,e) Cross-sectional SEM images showing the Cu layers on top of the d) TMPTA/PDD 90/10 and e) TMPTA/PDD 50/50 negative photopolymers. f) The thickness of the Cu layers on the negative photopolymer after 0.5 h deposition. g) Photograph showing the setup of four probe conductivity measurements and numbering of the measured strut positions on a fully Cu-plated octet truss lattice. h) The conductivity of the Cu layers measured on different struts of octet truss lattices printed with the negative resins. i,j) Microscopic images of the Cu layers on the TMPTA/PDD h) 90/10 and i) 50/50 photopolymers.

Using energy-dispersive spectroscopy (EDS) which is more bulk sensitive,^[30] the atomic percentage of Pd particles showed their coherence with the PDD content, i.e., a higher PDD content anchored more Pd as shown in Figure 2j and Table S3 (Supporting Information).

The difference in the distribution of Pd nanoparticles was governed by the different crosslinking densities determined by the resin formula, as illustrated in Figure 2k,l. We observed from Figure S3 (Supporting Information) that the resins absorbed a higher amount of water as the PDD content increased, which means that the water-borne Pd(II) can permeate deeper inside the resin to complex with the negatively charged sites underneath the surface. The in situ reduction merged the adjacent Pd(II) into nanoparticles with larger sizes embedded deeper inside the photopolymers. For the low PDD-content sample, the surface was densely cross-linked, less hydrophilic, and less charged. Such surface properties restricted the adsorption of Pd(II) to a limited amount and depth. Therefore, the Pd(II) could be only reduced into smaller particles anchored close to the surface. The smaller particle size observed from the photopolymer with a low PDD content is preferred in catalysis^[31] as it exposes a higher specific surface area with a better uniformity to promote the quality of Cu deposition. Moreover, considering the price of the noble metal Pd, the deeply embedded nanoparticles within the higher PDD

content photopolymers are a waste of materials as they cannot be accessed by the following Cu deposition reaction.

3.3. The 3D Patterning of Copper with High Fidelity and Conductivity

The immobilized Pd nanoparticles in situ catalyzed the Cu reduction on the negatively charged area (Figure 3a). Therefore, the catalyst-embedded negative photopolymers directly affected the properties of the deposited Cu layer.

Resolution is a crucial parameter for 3D printing. Using the projection stereolithography technique, we achieved a high resolution of Cu patterning in both the printing plane and the vertical direction. Figure 3b shows a clear boundary between the neutral and the Cu-coated negative photopolymers in the printing direction (z-direction). Figure 3c shows the finest feature size with accurately deposited Cu is 18 µm in the x-y plane which is equivalent to the smallest pixel size our projection stereolithography system can reach. The atomic force microscopy (AFM) height image in Figure S5 (Supporting Information) shows that the plated Cu layer had a dense and smooth surface with a R_a of 21.7 nm over a $10 \times 10 \mu\text{m}^2$ area, suggesting a good continuity of the Cu layer. The boundaries of Cu coating were clear without

cross-contamination in both the x - y plane and the z direction, showing excellent selectivity and precision of the Cu deposition in the 3D coordination. The cross-sectional SEM images in Figure 3d,e unveil that the Cu layers closely adhered to the resin substrates without noticeable gaps. The Cu coatings had good adhesion to the negative resins. All the coatings had minimal damaged areas after the tape tests and rated 4B (Figure S6, Supporting Information) which may benefit from the surface roughness created by the embedded Pd nanoparticles. In comparison, the conventional Cu-coated PEGDA sample rated only 2B (Figure S6, Supporting Information). Such a good coherence between the metal and the polymer promises the deposition resolution to be as precise as the printing resolution.

Though no selectivity difference was observed, varying the compositions of the negative resins did lead to different growth kinetics and textures of the cladding Cu, which was induced by the Pd distributions on the resin surfaces. The TMPTA/PDD 90/10 photopolymer had the finest Pd nanoparticles evenly dispersed on the surface and catalyzed the Cu deposition with optimal kinetics and best uniformity. A controlled and nearly linear growth in thickness of the dense Cu layer (Figure 3d) was estimated at $\approx 1.2 \mu\text{m h}^{-1}$. By increasing the PDD content, the Cu layers grew faster in thickness but with more pores (Figure 3e,f). As depicted in Figure 3g,h, we measured conductivity on fully Cu-plated all-negative-resin-printed octet truss lattices and evaluated the plating quality per resin composition. The octets printed with the same negative resin showed similar conductivity despite the position of the measured strut, indicating good uniformity throughout the 3D structure. TMPTA/PDD 90/10 delivered the highest conductivity of $4.9 \times 10^7 \text{ S m}^{-1}$ which was comparable with the electrical conductivity of annealed bulk Cu (see measurement details in the Supporting Information) and indicated the highest quality of the selectively deposited Cu layer. With an increasing PDD content, however, we noted a trend that the Cu cladding became less conductive as the TMPTA/PDD 50/50 photopolymer could only deliver a conductivity two orders of magnitude lower than TMPTA/PDD 90/10. The decrease can be mainly attributed to the more porous Cu layer generated by the heterogeneously distributed Pd nanoparticles. Besides, under a microscope, we observed an increased number of cracks on the Cu layer at different scales as the PDD content increased (Figure 3i,j; Figure S7, Supporting Information). The cracks are believed to be caused by the more significant swelling in the high-PDD-content photopolymers. After the plating process in the aqueous solution, the sample loses water and shrinks which is believed to have caused the cracking of the Cu layer.

3.4. Conductive/Dielectric 3D Architectures with Tunable Mechanical Properties — From Stiff to Flexible

The mechanical robustness of printed materials is the foundation of practical applications of 3D electronics, especially for lattice designs with reduced materials used. Tailoring materials' mechanical properties enable applications of electronics in different conditions.

For the negative photopolymers with different proportions of TMPTA/PDD in this work, their high cross-link densities owing

to the higher proportion of TMPTA lead to rigid mechanical properties. Table 1 and Figure S8 (Supporting Information) show that a higher content of TMPTA increased the stiffness and brittleness of the photopolymers. With a TMPTA proportion higher than 70%, the samples gave linear elastic responses without yielding and had similar Young's modulus as high as $1.05 \pm 0.01 \text{ GPa}$. The addition of PDD induced a characteristic plastic deformation due to the decreased crosslinking density. When the PDD content was less than 30%, increasing the proportion of PDD did not change Young's modulus but only elongated the elastic response region from $2.98 \pm 1.09\%$ to $7.95 \pm 1.74\%$, thus leading to higher strength of $59.92 \pm 9.37 \text{ MPa}$ and toughness of $2.79 \pm 0.79 \text{ MJ m}^{-3}$. When the PDD content was further increased to 40% and 50%, a characteristic stress-strain response of ductile plastic materials was observed and the Young's modulus dropped to $0.83 \pm 0.01 \text{ GPa}$ and $0.34 \pm 0.04 \text{ GPa}$, respectively. The high PDD concentration substantially decreased the crosslinking density, making the photopolymer less resilient to deform. By changing the proportion of TMPTA/PDD, a series of materials with high stiffness or ductility could be prepared.

To further explore the potential of charge-programmed selective plating in flexible electronics, a mono-functional photo monomer, PA, was selected to formulate a flexible negative resin with PDD (Figure 4a). PA has a phenyl group with a large stereo hindrance and thus coils its amorphous linear polymer chain, which can be stretched to a large deformation upon external stress. PDD acted not only as the charge carrier but also as the cross-linker in this system because it has two carbon–carbon double bonds for photopolymerization. To reserve the flexibility to the largest extent, the amount of PDD was kept at 5% to moderately cross-link the polymer chains of PA. As shown in Figure 4b and Table 1, the PA/PDD 95/5 photopolymer was highly flexible with a breaking elongation as high as $313.80 \pm 64.09\%$ and a Young's modulus of $0.91 \pm 0.10 \text{ MPa}$. The modulus is comparable to human skin (0.85 MPa),^[32] promising a potential application in electronic skins. Distinct from the TMPTA/PDD system, PA/PDD could be selectively plated with Cu at a ratio of 95/5, which further pushed the threshold of the PDD content to 5%. This is because, as compared to the TMPTA/PDD photopolymers PA/PDD had a less cross-linked surface, allowing sufficient Pd(II) to permeate into the bulk, and accumulate into Pd nanoparticles with catalytic activity. The successful integration of charge-programmed selective plating to flexible substrates indicates this approach can be adapted to different polymer systems with variable mechanical properties.

To match the high elongation of the PA/PDD photopolymer, a liquid metal, gallium-indium eutectic (EGaIn), was introduced to the flexible negative system (Figure 4c). EGaIn is in a liquid state at ambient conditions, allowing large deformation while maintaining the structural continuity and consequently a metallic electrical conductivity. Gallium reactively wets Cu by forming the CuGa₂ alloy.^[33] Therefore, in an acidic environment, EGaIn spontaneously wets the surface of Cu without spreading onto the polymer surface due to its high surface energy. In such a way, we achieved the selective plating of EGaIn on the Cu-coated flexible negative photopolymer (Figure 4c). Upon a large deformation, the Cu layer broke but the EGaIn maintained a continuous conduct charge which is schematically shown in Figure 4d. Figure 4e,f shows that the EGaIn-coated flexible photopolymer

Table 1. Mechanical properties of the photopolymers with different compositions.

Resin composition	Mass ratio (wt./wt.)	Young's modulus (GPa)	Breaking elongation (%)	Strength (MPa)	Toughness (MJ m^{-3})
TMPTA/PDD	90/10	1.02 ± 0.05	2.98 ± 1.09	24.77 ± 6.35	0.44 ± 0.27
	80/20	0.98 ± 0.03	4.36 ± 1.61	34.87 ± 10.54	0.91 ± 0.64
	70/30	1.05 ± 0.01	7.95 ± 1.74	59.92 ± 9.37	2.79 ± 0.79
	60/40	0.83 ± 0.01	9.22 ± 1.91	46.52 ± 4.12	2.68 ± 0.46
	50/50	0.34 ± 0.04 (MPa)	10.74 ± 2.87	22.44 ± 2.75	1.58 ± 0.65
PA/PDD	95/5	0.91 ± 0.10	313.80 ± 64.09	1.32 ± 0.34	1.47 ± 0.43
	90/10	3.06 ± 0.14	52.15 ± 1.48	1.59 ± 0.09	0.43 ± 0.02
	80/20	8.99 ± 1.01	39.66 ± 4.93	3.80 ± 0.79	0.75 ± 0.23

maintained conductivity throughout at least 90 cycles of repeated stretching between 10% and 50% strain. The force and resistance were stabilized after 20 cycles and the resistance was maintained at an ultralow level $\approx 0.2 \Omega$ during the entire test. Without EGaIn, the Cu-coated flexible negative photopolymer lost the electrical conductivity upon a lateral stretch of 22% elongation (Figure S9, Supporting Information). The combination of the selective deposition of 3D printed flexible substrates and the EGaIn offered a platform where liquid state EGaIn can be precisely shaped into 3D sophisticated patterns with the conductivity of a metal and

flexibility of a liquid, which has never been realized before by any techniques.

The diverse mechanical properties of the resins promised a broad range of choice of materials. We demonstrated ultra-stiff materials with modulus in the order of gigapascal (1.05 ± 0.01 GPa) and ultra-soft materials with slightly higher modulus than skin (0.91 ± 0.10 MPa) with metals meticulously chosen to match the modulus. Our method is also compatible with selective deposition on polyimide^[25] and ceramic, both of which are known for excellent thermal resistance and

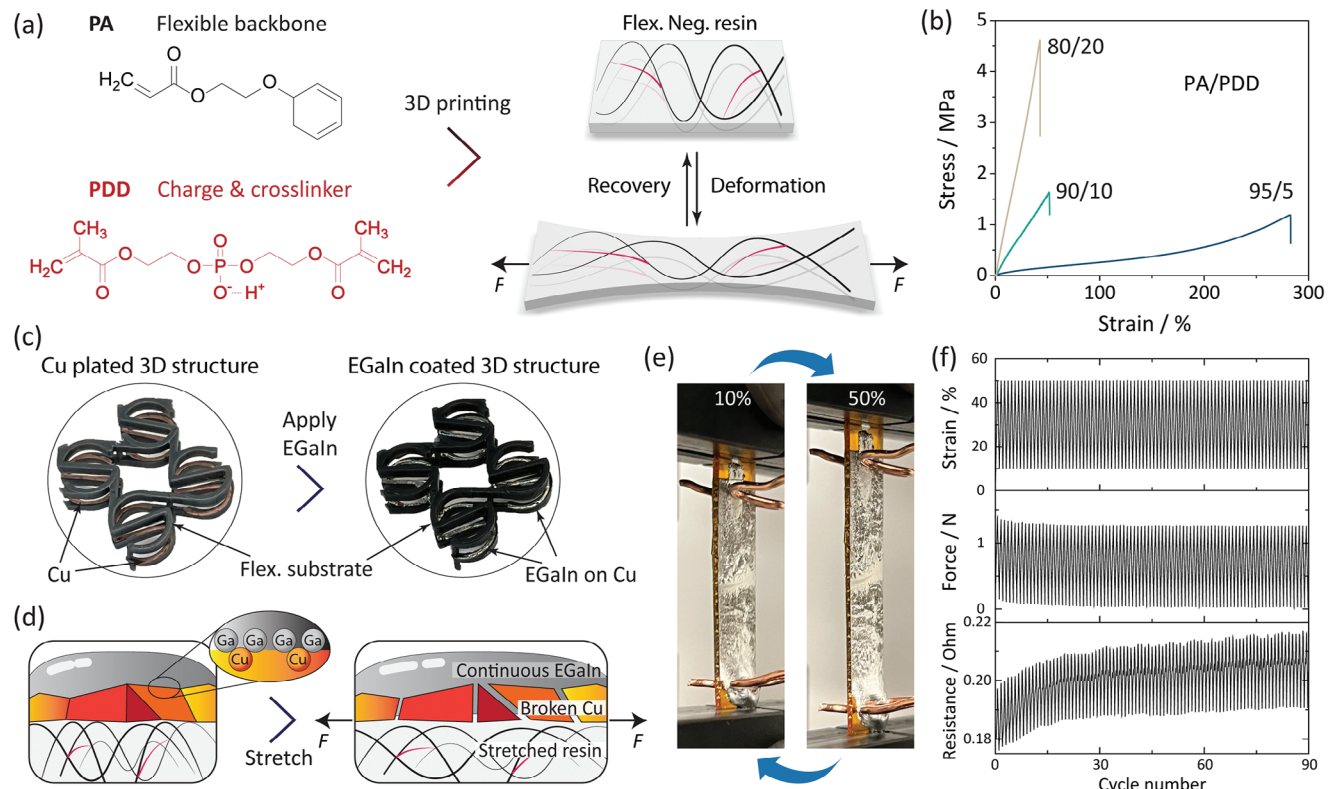


Figure 4. Selective metal deposition on flexible substrates. a) Chemical composition of the flexible negative resin and schematic illustration of the configuration change of the printed polymer chains upon stretching. b) Stress-strain curves of the flexible negative PA/PDD photopolymers. c) Photographs showing the selective wetting of EGaIn on the Cu-patterned 3D flexible unit cells of the antenna. d) Cross-sectional schematic illustration showing the maintenance of electrical conductivity by the EGaIn-coated flexible negative strip upon stretching. e) Photos and f) measured deformation, force, and resistance of the EGaIn-coated flexible negative strip being repeatedly stretched for 90 cycles.

outstanding dielectric properties. Figure S10 (Supporting Information) demonstrates a 3D printed S-ring pattern of a transmittarray on polyimide and a selectively Cu-coated ceramic. These results strongly indicate the versatility of the selective metal deposition approach and its promising potential for broader applications.

3.5. Light-Weight and Deployable Antenna

Developing antennas that are lightweight and deployable can notably extend their usage to aerospace applications beyond conventional uses in radar and communications, enabling scientific missions and communications via low-cost, small-form-factor platforms such as CubeSats.^[34] Our selective Cu deposition precisely integrates dielectric polymers with tunable mechanical properties and highly conductive metals into 3D complex structures which naturally provides a platform for designing deployable light-weight antennas. Herein, we demonstrate an example of an all-3D-printed antenna system comprised of a horn feed and a transmittarray that were both 3D printed and selectively coated with Cu on the designated areas.

First, we designed and 3D printed the horn antenna with the negative resin TMPTA/PDD 70/30 with its inner surface selectively deposited with Cu, as shown in Figure S11 (Supporting Information). This horn is designed to generate circularly polarized radiation through its flaring cone,^[35] and can be used as the feed source to illuminate a transmittarray antenna. The horn had a five-stage septum polarizer in the middle as shown in Figure S11 (Supporting Information) for generating high-purity circular polarization in a wide bandwidth.^[36] A built-in meandered waveguide was used as the transition between the excitation source and the open port of the polarizer. We precisely 3D printed the sophisticated structured horn body with the negative resin and plated conformal Cu on the interior surface. We evaluated the horn's performance at 19 GHz in UCLA's spherical near-field antenna measurement range (Figure S11, Supporting Information). The measured radiation pattern was in good agreement with the simulation with the loss measured to be 1.6 dB. The loss is at a similar level to other horn antennas fabricated using 3D printing followed by metallization.^[37] The results indicate the accuracy of charge-programmed 3D printing and the sufficient quality of the plated Cu and promise the application of the horn as the feed source for a more complex antenna system.

For horn antennas, due to the "skin effect," alternating current is dominantly distributed within several skin depths beneath the surface of the metal (skin depth in copper at 19 GHz is $\approx 0.47 \mu\text{m}$).^[38] This implies the possibility of building complex horn antennas with lightweight polymers and proper conductive coating. Taking advantage of this feature, the weight of conventional all-metal horns could be largely reduced by replacing the unnecessary thickness of metal with lightweight polymers. We plated the horn with a Cu cladding of 1 μm thick (Figure S12, Supporting Information) that was highly uniform and continuous despite the structural complexity of the horn antenna. Our antenna weighed 12 g, which was only 13% of the mass if the same horn were to be built with bulk bronze. The reduction of Cu usage not only cut the weight of the antenna but also lowered the materials expense considering the relatively high price of Cu.

It should be noted that the extended Cu-plating time required excellent structural stability from the photopolymer to resist swelling as the inner chamber of the horn had to be in contact with the deposition liquid for a long time. Here, we select TMPTA/PDD 70/30 to print the horn, considering its highest toughness and strength among all compositions. In comparison, a horn printed with TMPTA/PDD 50/50 was swollen significantly and leaked the Cu deposition solution (Figure S13, Supporting Information). Eventually, the crevices resulted in rupture. The phenomenon highlights the significance of balancing the crosslink and charge densities of the negative photopolymers as this ratio affected not only the selective plating efficiency but also the performances of the printed electronic devices.

Using the negative flexible resin, we printed a deployable transmittarray with an aperture of 12 cm (Figure 5a,b) consisting of three stacked layers (Figure 5c). This design is a direct carry-over from the previous successful transmittarray design using rigid PEGDA (see details in Figure S14a, Supporting Information).^[39] Each layer has 208 "S-ring" elements that were precisely coated with Cu using selective deposition, and the same pattern is repeated and strictly aligned for all three layers in order to provide the desired electromagnetic wave transmission efficiency. Each of the S-ring elements was rotated by a unique angle such that the transmittarray, when illuminated by the feed horn (low gain), can compensate the spherical incident phase front into a uniform aperture phase at the transmitted side to achieve more directive radiation (higher gain). The original design was 3D printed using the same charge-programmed deposition with rigid PEGDA as the neutral dielectric and TMPTA/PDD as the negative charge resin (Figure S14b, Supporting Information) which gave a directivity of 24.1 dB, corresponding to an aperture efficiency of 45.1%.^[39] To achieve flexibility, as shown in Figure 5d, we redesigned the connection between the unit cells to be reconfigurable so that the transmittarray could fold and deploy. The as-prepared flexible transmittarray was measured at 19 GHz and showed a similar radiation pattern as the simulation results (Figure 5e,f). This low-profile transmittarray antenna allows focusing electromagnetic waves into a high-gain beam which is enabled by its unprecedented 3D complexity, resolution, alignment, and precision in patterning the metal and dielectric features. The success in creating a high-gain beam presents promising possibilities in the design and manufacturing of flexible and deployable antenna devices. The deployability is based on a lightweight antenna structure with minimal in-plane constraints and materials flexibility. In contrast, conventional deployable antennas save volume or area via paper folding or origami with one layer of simple patterns which is insufficient to realize phase compensation to focus electromagnetic beams.^[40] Unfolding those antennas required a specific mechanism to flatten the patterns on the thin film substrates where minimal dislocation is inevitable. They typically only function as directional antennas for communication and CubeSat applications below 5 GHz.^[40] After five fold/deploy cycles, though the measured directivity dropped from 17.8 to 15.4 dBi, our flexible transmittarray still demonstrated a good resemblance to the pattern before folding as shown in Figure 5g, indicating the robustness of the flexible transmittarray. Figure 5g shows that the light weight of the printed polymer made the flexible transmittarray 83% lighter than the same design that was previously fabricated on a printed circuit board (PCB).^[11] The

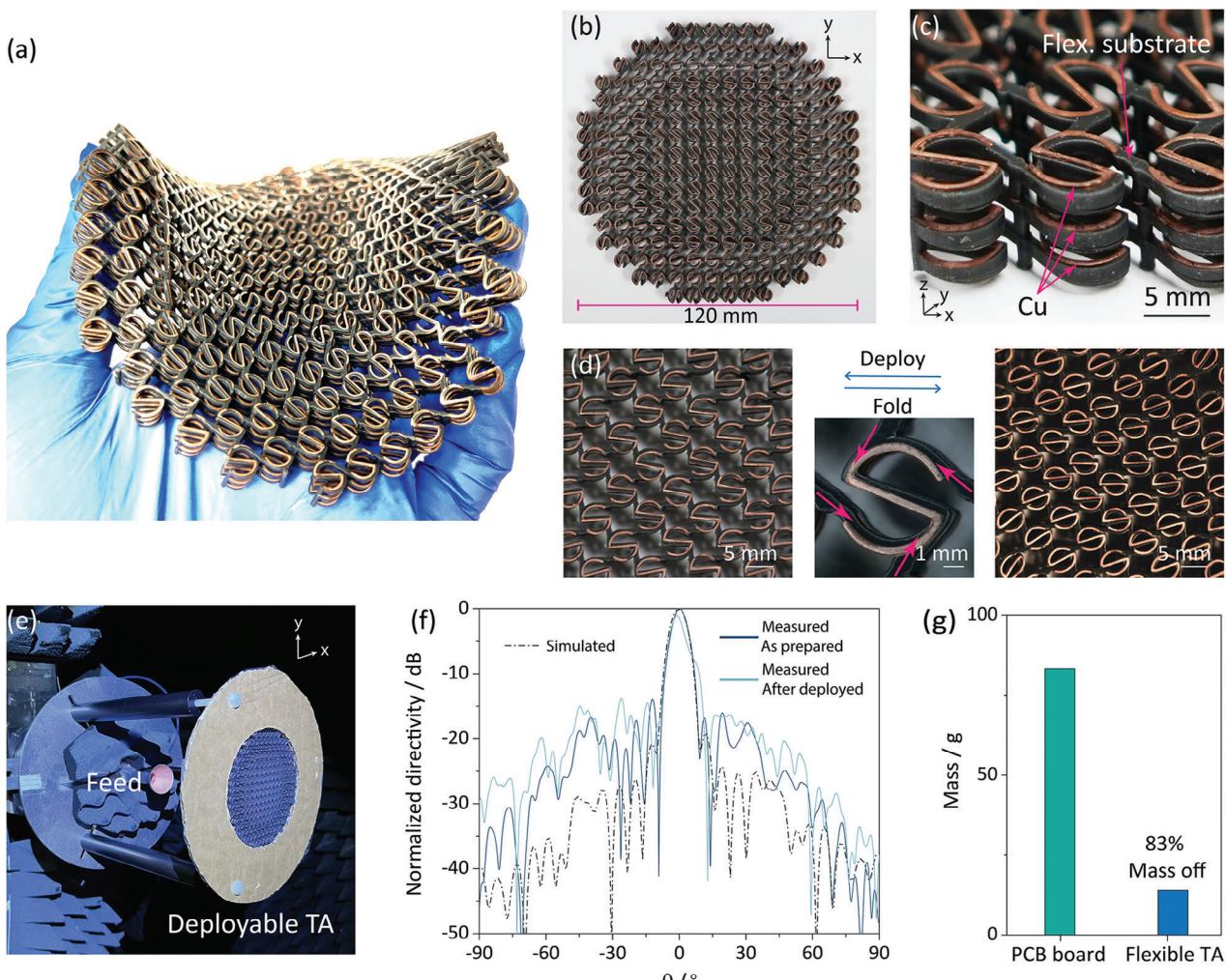


Figure 5. The 3D printed flexible antenna system. a,b) Photograph of the flexible transmitarray with S-rings selectively coated with Cu. c) Photograph showing the three-layer structure of the flexible transmitarray. d) Photographs showing the flexible transmitarray when deployed and folded. e) Photograph showing the 3D printed flexible antenna being measured. f) The simulated and measured radiation patterns of the flexible transmitarray before and after being deployed. g) Mass comparison of the flexible transmitarray versus one printed on a PCB.^[11]

Cu coating on compatible dielectrics also showed excellent resilience to temperature change. Figure S15 (Supporting Information) shows the resistance change of Cu on TMPTA/PDD 70/30 and polyimide. After three cycles of freezing (-20°C , 35%–40% relative humidity) and heating (270°C), the Cu layer decreased its resistance by 9% and 8%, respectively, possibly due to the Cu particles being further sintered at the high temperature. The significantly reduced mass and thermal stability are advantageous for deep space missions.^[34a,41]

4. Conclusion

In this work, we demonstrated a class of spatially 3D patterned conductive and dielectric architectures with a wide range of mechanical stiffness via 3D printing a series of photo-curable resins carrying tunable crosslink densities and charge polarities. A higher crosslink density led to a rigid network with en-

hanced structural stability against swelling, but also induced brittleness. At a certain crosslink density, a minimal amount of charge monomers accommodated the catalyst particles close to the surface with finer sizes favoring catalytic efficiency for the subsequent metal depositions. Based on these fundamental investigations, we selectively pattern metals on 3D architectures matching a wide range of stiffness (modulus ranging from 1.05 GPa to 0.9 MPa) via tailoring the molecular structures of the charged resins. With optimizations on the charge programmed deposition process and the structure of the charged monomers, we report a very high electrical conductivity of $4.9 \times 10^7 \text{ S m}^{-1}$ for the 3D patternable Cu, with high uniformity and precision, plus variable flexibility enabled by selective patterning of liquid metal. As a potential application, we took advantage of the charge programmed 3D printing technique in fabricating electronics with unprecedented complexity and precision of interpenetrating dielectric and conducting phases and demonstrated

a deployable light-weight all-3D-printed antenna system comprised of a horn feed source and a flexible transmitarray featured with structurally optimized lattice architectures in multiple layers. Our approach results in over 80% weight reduction of the antennas compared to traditionally manufactured counterparts. Additionally, we demonstrated that the flexible transmitarray was functional after folding (e.g., for compact transport packaging) and deployment (i.e., unfolding into the designed configuration). The reduced mass and volume as well as variable mechanical flexibility make such antenna systems prospective candidates for small satellite and CubeSat antennas that necessitate the stowage and deployment of lightweight large-aperture antennas. This work provides materials design principles for a novel charge-programmed additive manufacturing technique, which enabled 3D patterned conductive and dielectric architectures with broad spatial complexity. This approach can find a myriad of electronic applications, including antennas, soft robotics, and metamaterials where structural, functional, and embedded 3D electrode interfaces are tightly integrated.

Supporting Information

Supporting Information is available from the Wiley Online Library or from the author.

Acknowledgements

The authors would like to acknowledge the NSF CAREER award (2048200), Office of Naval Research (N00014-23-1-2797) and DARPA Young Faculty Award for funding support of this work.

Conflict of Interest

The authors declare no conflict of interest.

Data Availability Statement

The data that support the findings of this study are available from the corresponding author upon reasonable request.

Keywords

3D printing, electronics, metal deposition, photopolymers, selectivity

Received: November 5, 2023
Published online:

- [1] M. R. M. Hashemi, A. C. Fikes, M. Gal-Katziri, B. Abiri, F. Bohn, A. Safarpour, M. D. Kelzenberg, E. L. Warmann, P. Espinet, N. Vaidya, E. E. Gdoutos, C. Leclerc, F. Royer, S. Pellegrino, H. A. Atwater, A. Hajimiri, *Nat. Electron.* **2019**, *2*, 195.
- [2] H. Cui, D. Yao, R. Hensleigh, H. Lu, A. Calderon, Z. Xu, S. Davaria, Z. Wang, P. Mercier, P. Tarazaga, X. R. Zheng, *Science* **2022**, *376*, 1287.
- [3] A. Hajiaghajani, A. H. Afandizadeh Zargari, M. Dautta, A. Jimenez, F. Kurdahi, P. Tseng, *Nat. Electron.* **2021**, *4*, 808.

- [4] A. W. Topol, D. C. L. Tulipe, L. Shi, D. J. Frank, K. Bernstein, S. E. Steen, A. Kumar, G. U. Singco, A. M. Young, K. W. Guarini, M. Ieong, *IBM J. Res. Dev.* **2006**, *50*, 491.
- [5] N. Liu, H. Guo, L. Fu, S. Kaiser, H. Schweizer, H. Giessen, *Nat. Mater.* **2008**, *7*, 31.
- [6] M. Zhang, H. Mei, P. Chang, L. Cheng, *J. Mater. Chem. A* **2020**, *8*, 10670.
- [7] B. Wu, A. Kumar, *Appl. Phys. Rev.* **2014**, *1*, 011104.
- [8] Y. Dong, C. Bao, W. S. Kim, *Joule* **2018**, *2*, 579.
- [9] J.-C. S. Chieh, B. Dick, S. Loui, J. D. Rockway, *IEEE Antennas Wirel. Propag. Lett.* **2014**, *13*, 201.
- [10] P. Wang, J. Li, G. Wang, Y. Hai, L. He, Y. Yu, X. Wang, M. Chen, B. Xu, *ACS Appl. Mater. Interfaces* **2022**, *14*, 28060.
- [11] A. Papathanasopoulos, J. Wang, Y. Rahmat-Samii, in 2021 Antenna Measurement Techniques Association Symp. (AMTA), IEEE, New York **2021**, pp. 1.
- [12] E. Macdonald, R. Wicker, *Science* **2016**, *353*, aaf2093.
- [13] E. Macdonald, R. Salas, D. Espalin, M. Perez, E. Aguilera, D. Muse, R. B. Wicker, *IEEE Access* **2014**, *2*, 234.
- [14] T. D. Ngo, A. Kashani, G. Imbalzano, K. T. Q. Nguyen, D. Hui, *Composites Part B* **2018**, *143*, 172.
- [15] S. C. Ligon, R. Liska, J. Stampfli, M. Gurr, R. Mühlaupt, *Chem. Rev.* **2017**, *117*, 10212.
- [16] T. Debroy, H. L. Wei, J. S. Zuback, T. Mukherjee, J. W. Elmer, J. O. Milewski, A. M. Beese, A. Wilson-Heid, A. De, W. Zhang, *Prog. Mater. Sci.* **2018**, *92*, 112.
- [17] a) J. Zhan, T. Tamura, X. Li, Z. Ma, M. Sone, M. Yoshino, S. Umezu, H. Sato, *Addit. Manuf.* **2020**, *36*, 101556; b) K. Song, Y. Cui, T. Tao, X. Meng, M. Sone, M. Yoshino, S. Umezu, H. Sato, *ACS Appl. Mater. Interfaces* **2022**, *14*, 46896.
- [18] S. Lee, M. Wajahat, J. H. Kim, J. Pyo, W. S. Chang, S. H. Cho, J. T. Kim, S. K. Seol, *ACS Appl. Mater. Interfaces* **2019**, *11*, 7123.
- [19] a) J. Zhang, J. Feng, L. Jia, H. Zhang, G. Zhang, S. Sun, T. Zhou, *ACS Appl. Mater. Interfaces* **2019**, *11*, 13714; b) J. Li, Y. Zhang, P. Wang, G. Wang, Y. Liu, Y. Liu, Q. Li, *ACS Appl. Mater. Interfaces* **2021**, *13*, 22891; c) P. Wang, J. Li, G. Wang, L. He, J. Yang, C. Zhang, Z. Han, Y. Yan, *Addit. Manuf.* **2023**, *63*, 103388.
- [20] K. Angel, H. H. Tsang, S. S. Bedair, G. L. Smith, N. Lazarus, *Addit. Manuf.* **2018**, *20*, 164.
- [21] N. Lazarus, J. B. Tyler, J. A. Cardenas, B. Hanrahan, H. Tsang, S. S. Bedair, *Addit. Manuf.* **2022**, *55*, 102793.
- [22] R. Hensleigh, H. Cui, Z. Xu, J. Massman, D. Yao, J. Berrigan, X. Zheng, *Nat. Electron.* **2020**, *3*, 216.
- [23] D. Helena, A. Ramos, T. Varum, J. N. Matos, *IEEE Access* **2020**, *8*, 177064.
- [24] X. Zheng, H. Lee, T. H. Weisgraber, M. Shusteff, J. Deotte, E. B. Duoss, J. D. Kuntz, M. M. Biener, Q. Ge, J. A. Jackson, S. O. Kucheyev, N. X. Fang, C. M. Spadaccini, *Science* **2014**, *344*, 1373.
- [25] J. Herzberger, V. Meenakshisundaram, C. B. Williams, T. E. Long, *ACS Macro Lett.* **2018**, *7*, 493.
- [26] H. Lu, H. Cui, G. Lu, L. Jiang, R. Hensleigh, Y. Zeng, A. Rayes, M. K. Panduranga, M. Acharya, Z. Wang, A. Irimia, F. Wu, G. P. Carman, J. M. Morales, S. Puttermann, L. W. Martin, Q. Zhou, X. Zheng, *Nat. Commun.* **2023**, *14*, 2418.
- [27] a) Z. Xu, C. S. Ha, R. Kadam, J. Lindahl, S. Kim, H. F. Wu, V. Kunc, X. Zheng, *Addit. Manuf.* **2020**, *32*, 101106; b) Z. Xu, R. Hensleigh, N. J. R. K. Gerard, H. Cui, M. Oudich, W. Chen, Y. Jing, X. Zheng, *Addit. Manuf.* **2021**, *47*, 102321.
- [28] X. Zheng, W. Smith, J. Jackson, B. Moran, H. Cui, D. Chen, J. Ye, N. Fang, N. Rodriguez, T. Weisgraber, C. M. Spadaccini, *Nat. Mater.* **2016**, *15*, 1100.
- [29] M. C. Biesinger, B. P. Payne, L. W. M. Lau, A. Gerson, R. S. C. Smart, *Surf. Interface Anal.* **2009**, *41*, 324.

- [30] K. A. Wepasnick, B. A. Smith, K. E. Schrote, H. K. Wilson, S. R. Diegelmann, D. H. Fairbrother, *Carbon* **2011**, *49*, 24.
- [31] L. Liu, A. Corma, *Chem. Rev.* **2018**, *118*, 4981.
- [32] P. G. Agache, C. Monneur, J. L. Leveque, J. De Rigal, *Arch. Dermatol. Res.* **1980**, *269*, 221.
- [33] Y. Cui, F. Liang, Z. Yang, S. Xu, X. Zhao, Y. Ding, Z. Lin, J. Liu, *ACS Appl. Mater. Interfaces* **2018**, *10*, 9203.
- [34] a) Y. Rahmat-Samii, V. Manohar, J. M. Kovitz, *IEEE Antennas Propag. Mag.* **2017**, *59*, 22; b) J. Wang, V. Manohar, Y. Rahmat-Samii, *IEEE Antennas Propagat. Mag.* **2021**, *63*, 14.
- [35] W. L. Stutzman, G. A. Thiele, *Antenna Theory and Design*, Wiley, Hoboken, NJ **1998**.
- [36] Ming Chen, G. Tsandoulas, *IEEE Transact. Antennas Propag.* **1973**, *21*, 389.
- [37] C. R. Garcia, R. C. Rumpf, H. H. Tsang, J. H. Barton, *Electron. Lett.* **2013**, *49*, 734.
- [38] a) Z. Tao, V. Subramanian, H. Portela, G. Boeck, in *2009 SBMO/IEEE MTT-S Int. Microwave Optoelectronics Conf. (IMOC)*, IEEE, New York **2009**, pp. 92; b) J. Teniente, J. C. Iriarte, R. Caballero, D. Valcazar, M. Goni, A. Martinez, *IEEE Antennas and Wireless Propagation Letters* **2018**, *17*, 2070.
- [39] J. Wang, R. Hensleigh, Z. Xu, Z. Wang, X. Zheng, Y. Rahmat-Samii, in *2022 IEEE Int. Symp. Antennas Propagation USNC-URSI Radio Science Meeting (AP-S/URSI)*, IEEE, New York **2022**, pp. 645–646.
- [40] S. I. H. Shah, S. Bashir, M. Ashfaq, A. Altaf, H. Rmili, *IEEE Access* **2021**, *9*, 86429.
- [41] S. Jacobs, C. Coconnier, D. Dimaio, F. Scarpa, M. Toso, J. Martinez, *Smart Mater. Struct.* **2012**, *21*, 075013.